Calculating X-ray absorption near-edge structure at very low energy

Yves Joly

Laboratoire de Cristallographie, CNRS, Associé à l'Université Joseph Fourier, BP 166, F-38042 Grenoble CEDEX 9, France. E-mail: yves.joly@polycnrs-gre.fr

The measurement and calculation of X-ray absorption near-edge structure at very low energy can provide important information about a metallic center in biological compounds. A rapid overview of the biological applications of this technique is given, then a new method of calculating the spectra is presented. This technique, based on the use of the finite-difference method to solve the Schrödinger equation, is especially precise and potentially applicable to metalloproteins. Examples of its use on an oxide and an organic compound illustrate the kind of spectroscopic information that can be obtained.

Keywords: X-ray absorption near-edge structure (XANES); low energy; biological compounds.

1. Introduction

The impact of structural biology in all areas of biological science has expanded greatly. These advances are attributed to important improvements in the ability to clone a vast array of cellular proteins and to crystallize them, while the technological innovations at synchrotron radiation facilities have permitted the collection of data that would have been unreachable a few years ago. In this area, most of the results are obtained by diffraction techniques; nevertheless, complementary information is also obtained by spectroscopic methods such as X-ray absorption spectroscopy (XAS). For example, X-ray crystallography and XAS in combination provide a complete description of metal sites in proteins, which is not provided by either technique alone. This fact is important because metalloproteins are involved in all biological energy capture, conversion and transfer. XAS spectra are frequently divided into the regions of X-ray absorption near-edge structure (XANES), within about 50 eV of the edge, and extended X-ray absorption fine structure (EXAFS), from about 50 eV to 1000 eV above the edge. The EXAFS region provides structural information about the absorbing atom and can be analyzed to give precision in bond lengths down to ± 0.02 Å. The XANES region contains information about the oxidation state and local geometry of the absorbing atom. Therefore, particular attention is often given to the lowest-energy part of the spectrum, that is, the first few electron-volts around the edge. This analysis, currently more frequently performed in solid state physics, is of growing interest for the study of biological compounds. Typical features and thus typical sensitivity to electronic and geometrical parameters are present in this energy range. This is due to the fact that the photoelectron has sufficiently low kinetic energy to make it sensitive to the details of the potential shape and thus to the details of the electronic structure.

In the next section, biological examples of low-energy XANES analysis will be presented. A recently developed way of calculating X-ray absorption using the finite-difference method (FDM) is then described. This method, which is supposed to be especially precise and is suitable for future adaptation for use with biological compounds, is applied in §4 to an oxide and an organic molecule.

2. Pre-edge analysis of biological compounds

2.1. Low-energy edges

The most promising developments for the use of XANES concern metalloprotein applications because of the small number of metallic atoms present in these giant molecules. Nevertheless, when their fundamental building blocks (amino acids) are considered instead, the number of small-Z atoms becomes sufficiently low to make the analysis around their K-edge relevant. Therefore, for instance, Boese and Carravetta have studied experimentally (Boese *et al.*, 1997) and theoretically (Carravetta *et al.*, 1998) the C K-edge XANES spectra of amino acids. Tanaka *et al.* (2001) have measured the O K-edges of the same compounds, that is, glycine, different alanines, asparic acid and tyrosine. The spectra were resolved using discrete variational $X\alpha$ calculations. The different antibonding π^* and σ^* orbitals were in this way identified in the XANES spectra, and the comparison of these structures, at least in the smallest amino acids, proved also to be possible.

Another example of small-Z-edge analysis is the determination of the metal–ligand charge distribution in molybdenium–sulfur compounds (Rompel *et al.*, 2001). There, the S K-edge and the Mo L-edge were measured in order to investigate the charge distribution between Mo and S in a series of molybdenium thiolate compounds. These serve as amide–sulfur hydrogen-bonding models and exhibit different redox potentials arising from polar-group effects and ligand–hydrogen bonds near the redox center. For all oxidized complexes, the S K-edge spectra exhibit a thiolate-based pre-edge feature centered at 2470.2 eV, and the inflection point occurs at 2472.0 eV. No intense pre-edge feature is observed in the spectra for the reduced Mo model compounds, and the energy shift of the S K-edge position depends on the S ligand. Correlations between ligand charge density and the redox potential of the Mo—S cores are observed.

2.2. Oxidation-state studies of 3*d* transition-metal compounds

One of the most common XANES studies in biological science concerns the analysis of the oxidation states of the 3d metal atoms. These atoms are present naturally or as pollutants in the environment. These analyses are often performed by a simple comparison with reference samples. In that context, the use of a microprobe beamline is often necessary to select very small samples. For instance, Illman *et al.* (1994) studied the redox states of chromium in wood treated with metal-based preservatives containing this element. Hexavalent chromium is toxic, in contrast to trivalent chromium, and the desired outcome from treating wood with chromate copper arsenate is a total change of Cr(VI) to Cr(III). Therefore, the authors determined the redox states of Cr *in situ* in treated southern yellow pine lumber. This was achieved by analyzing the strong pre-edge feature present in Cr(VI) but absent in Cr(III).

There is also an example of chromate study in the work of Park *et al.* (2000), the final goal being bioremediation to remove a chromate from the environment. The same conversion as above [chromate to Cr(III)] was quantitatively evaluated, with the same pre-edge feature analysis, during an enzyme reaction.

Another example of oxidation-state study can be found in the XANES measurement and analysis of a single neuron from a patient with Parkinson's disease by Yoshida *et al.* (2001). The chemical states of iron in the neuron of the *substantia nigra* are related to the oxidative damage leading to neuronal cell death. In that context, XANES results showed that iron changes from the ferrous (Fe^{2+}) to ferric (Fe^{3+}) ion in the process of neuron degeneration. In that study,

it is the chemical shift of the edge, compared with reference spectra, that allow the effect to be quantified.

The same class of investigation can be found in the single macrophage cell XAFS study of Kitamura & Ektessabi (2001). It is shown that metal elements absorbed by the cell interact with the cell and that the chemical state of the metal is changed.

Finally, oxidation-state analysis does not necessarily only involve the interpretation of the energy shift of the threshold. The slope of the edge can also be a signature of different oxidation conditions. For instance the Cu *K*-edge in the mushroom *Agaricus bisporus* tyrosinase in solution in the oxy and deoxy forms reveals their different oxidation state [Cu(II) and Cu(I), respectively] by the presence of a shoulder in the rising edge (Della Longa *et al.*, 1996).

2.3. Pre-edge evolution under beam irradiation

The study of pre-edge evolution is important in the control of radiation damage. For instance, Akamatsu & Yokoya (2001) have analyzed the XANES spectral change of 2-deoxy-D-ribose after irradiation at different energies around the O *K*-shell absorption edge. Differences are observed between irradiation at energies below, on or above the edge, suggesting different chemical changes.

A more dramatic effect is often observed after exposure to X-rays. For instance, Meinke *et al.* (2000) measured intact and photoreduced manganese complexes. A 150 s exposure is sufficient to change the edge shape completely. It can be noted that in this case the pre-edge does not change, only the main edge is shifted and modified in shape.

To conclude, it must be stressed that important progress in the control and preparation of metalloprotein samples has now been achieved. For instance, Ascone and co-workers have developed new electrochemical cells adapted to biological compounds (Giorgetti *et al.*, 2000). They have also used a saccharose matrix (Ascone, Sabatucci *et al.*, 2000), which protects the sample under the X-ray beam. The quality of this protection was checked by inspecting the edge shape of the sample.

2.4. Protein studies

Proteins have many conformation substates, and their identification is one element that is required in order to understand their dynamics. Modulation of the thermodynamic variables, like temperature (Della Longa *et al.*, 1994) and pressure (Ascone, Cognigni *et al.*, 2000), has been used during XAS measurements to identify these conformation states.

In the metalloprotein area, the lowest-energy part of the XAS spectra is rarely studied. One very interesting case concerns a polarized analysis of the photoproduct of carbon monoxymyoglobin (Della Longa *et al.*, 1999). It was shown that the XANES spectrum polarized in the direction along the Fe—CO bond changes dramatically after photolysis, while more subtle changes are observed in the spectrum polarized along the heme plane. Moreover, changes in the pre-edge region were analyzed during the photochemical reaction, and this provided insight into the electronic structure of the highest occupied and lowest unoccupied molecular orbitals. This kind of analysis, supported by quantitative calculations, can certainly be developed for biological compounds.

More conventional is the analysis of the structural changes in photosynthetic bacteria. They affect the electron transfer rate in reaction-center proteins (Chen *et al.*, 2000). However, the authors also analyze the presence of a pre-edge structure that could indicate a more distorted geometry.

Other examples of edge studies can be found in the Zn (Jacquamet *et al.*, 1998) and Co (Adrait *et al.*, 1999) *K*-edge studies in fur protein from *Escherichia coli*. The Co XANES presents a pre-edge that is analyzed by the authors in terms of a transition towards the 3*d* and 4*p* levels and is qualitatively connected to the coordination number.

This rapid overview of low-energy XANES applications to biological compounds is concluded by stating that, most often, analyses are qualitative. Quantitative analyses are more concerned with the higher-energy part of the spectrum. The purpose of the following section is to present a recent scheme of calculation that can provide access to spectroscopic analysis of the lowest-energy range.

3. A new scheme of calculation

3.1. The absorption cross section

In the one-electron quadrupolar approximation, neglecting spin for simplicity, the photoabsorption cross section resulting from a transition between initial core states ψ^g and final states ψ^f is given by

$$\sigma = 4\pi^2\alpha\hbar\omega \sum_{f,g} |\langle\psi^f|\varepsilon.\mathbf{r}(1 + 0.5i\,\mathbf{k}.\mathbf{r})|\psi^g\rangle|^2\,\delta(\hbar\omega - E_f + E_g),$$

where $\mathbf{k}$ is the photon wave vector and ε is the direction of the polarization. α is the fine structure constant, $\hbar\omega$ is the photon energy, and E_f and E_g are the final and initial state energies. The initial state can be represented by an atomic-core orbital that is easy to calculate. The summation over the final states to obtain the absorption cross section is also straightforward. In the *ab initio* calculation, the main difficulty resides in the evaluation of the final states, which is performed through different formalisms. The most famous methods make use of the multiple-scattering theory (MST) (Tyson *et al.*, 1992; Rehr *et al.*, 1992). Typically, MST employs an important approximation: the muffin-tin averaging of the potential needed for the expansion of the wavefunctions. In this approximation, the potential is spherically averaged in the atomic and outer-sphere regions and volumes are averaged in the interatomic region. The use of a constant interstitial potential is certainly a serious approximation, especially when the photoelectron kinetic energy is of the same order as the error in the value of the potential. Moreover, it leads to a dependence of the results on the size of the interstitial region itself. The restrictions imposed by the muffin-tin approximation can be lifted through a generalization of the multiple-scattering theory (Gonis *et al.*, 1989; Natoli *et al.*, 1986), but this has not yet been implemented. Various methods that can be applied to XANES have already tried to go beyond the muffin-tin approximation for energy-band problems. In particular, the discrete variational method (Ellis & Painter, 1970) uses a discretization of the potential to calculate matrix elements but keeps the usual expansion in plane waves in its Koringa–Kohn–Rostoker version. Ebert and co-workers (Huhne *et al.*, 1998), also using the Korringa–Kohn–Rostoker formalism in a full potential approach, have successfully applied the formalism to XANES (Ahlers, Attenkofer & Schütz, 1998; Ahlers, Schütz *et al.*, 1998; Huhne & Ebert, 1999). The full-linear augmented plane wave (FLAPW) approach (Blaha *et al.*, 1990) is also extensively used to calculate band structure without the muffin-tin approximation, but all of these methods are restricted to periodic potential. This point is a major difficulty for biological-compound applications.

The finite-difference method (FDM) is another way to solve the Schrödinger equation using the local-density approximation that avoids the muffin-tin averaging. The first formulation of the FDM to solve the Schrödinger equation was given in the 1930s by Kimball & Shortley (1934). Nevertheless, the FDM requires significant computing power and its progress has followed the improvements of computer capabilities. The purpose of the following section is to

describe the extension of this computing technique to XANES and to show the potential of the method in typical examples.

3.2. The finite-difference method

The FDM is a general way to solve differential equations by discretizing them over a grid of points in the volume where the calculation is made. In XANES, we are interested in the Schrödinger equation in a spherical volume centered on the absorbing atom and extending over a sufficiently large cluster.

Following Dill & Dehmer (1974), the space is divided into three regions: (i) an outer sphere surrounding the cluster of interest, (ii) an atomic region composed of very small spheres (up to 0.65 Å radius) around the atomic cores rather than the usual large muffin-tin spheres and (iii) the interatomic region where an FDM formulation of the Schrödinger equation is performed. In the outer-sphere region, the potential is assumed to be constant and a complete set of solutions is given by an expansion of the final states in spherical harmonics. Each final state f is now referenced by the kinetic energy of the photoelectron E in the outer sphere and a particular $L = (\ell, m)$ spherical wave attacking the cluster. Thus, the solutions are given by

$$\psi^{L,E}(\mathbf{r}) = (\kappa/\pi)^{1/2}\left[j_\ell(\kappa r)\, Y_L(\hat{\mathbf{r}}) + \sum_{L'} \tau_{L'}^{L,E}\, h_{\ell'}^{+}(\kappa r)\, Y_{L'}(\hat{\mathbf{r}}) \right],$$

where j_ℓ and h_ℓ^+ are the radial Bessel and Hankel outgoing functions. $\kappa = E^{1/2}$ is the electronic wave vector. The quantities $\tau_{L'}^{L,E}$ are the unknown cluster-scattering amplitudes to be determined in the way specified below. The factor $(\kappa/\pi)^{1/2}$, which is the vacuum state density, assures the normalization of the scattering wavefunction to one state per rydberg.

Since the potential is spherically symmetrical to a very good approximation in the atomic-core region, one can expand the solution as

$$\psi^{L,E}(\mathbf{r}) = \sum_{L'} A_{L'}^{L,E}\, R_{\ell'}^{E}(r)\, Y_{L'}(\hat{\mathbf{r}}),$$

where the functions $R_{\ell'}^{E}(r)$ are solutions of the radial Schrödinger equation inside the atoms, with the origin of the vector $\mathbf{r}$ taken at the atomic centers.

In the interatomic region, the unknowns are the values of the wavefunction on each grid point i: $\psi_i^{L,E} = \psi^{L,E}(\mathbf{r}_i)$. The Laplacian is obtained by approximating the wavefunction around the point i by a polynomial of order four. In this way, in an orthogonal frame, the Schrödinger equation becomes

$$[6 + h^2(V_i - E)]\psi_i^{L,E} - (16/15)\sum_{j}^{\text{first}} \psi_j^{L,E} + (1/15)\sum_{j}^{\text{second}} \psi_j^{L,E} = 0,$$

expressed in rydberg and atomic units. h is the interpoint distance; the smaller it is, the more accurate is the computation. $V_i = V(\mathbf{r}_i)$ is the potential on the node point i. The summations are over the six first- and the six second-neighbor points along the three orthogonal directions.

The amplitudes of the spherical harmonics within the atomic-core region and the outer sphere are evaluated using the continuity of the wavefunction and of its derivative between the different regions (Joly, 2001). Finally a large system of linear equations is obtained connecting the values of the wavefunction on all the grid points.

This formulation does not require any approximation on the shape of the potential, thus avoiding the problem related to the classical muffin-tin approximation. Moreover, the potential to a very good approximation can be assumed to be a function of the total electronic density relaxed around the core hole. The total electronic density can be calculated by self-consistent codes or, more simply, can be described by the superposition of the charge densities of the atoms whether neutral or ionized according to the system. In particular, bond-directed valence orbitals are used whenever appropriate.

Some practical examples of the use of this framework are given by Joly (2001).

3.3. Muffin-tin effects

In this section, we want to emphasize the effect of the muffin-tin approximation on the calculated XANES spectra.

The muffin-tin approximation corresponds to a monopolar representation of the potential. For this reason, it can be suspected that, with decreasing symmetry, non-muffin-tin effects must increasingly influence the signal. To check this assumption, numerical tests on small artificial iron oxide molecules were realized. Calculations on ordered and distorted FeO_6 octahedra were performed using muffin-tin (MT) and non-muffin-tin (NMT) calculations. Fig. 1 shows the calculations for a perfect octahedron. The Fe—O distance is 2.06 Å and the O—Fe—O angles are 90°. The symmetry is cubic and the agreement between MT and NMT calculations is very good. Curves are convoluted in the usual way, and there is a very good agreement with experiments performed on FeO_6 in solution. Then the octahedron is contracted along the z axis by 10%. There is a loss of two fourfold axes; the Fe atom remains at an inversion center. Fig. 2 shows the linear dichroism between the polarization parallel and perpendicular to the contraction. The difference between MT and NMT calculations is noticeable in the 0–50 eV range. In particular, the minimum at around 40 eV is shifted, which could be interpreted as a smaller contraction. The effect can probably be diminished with a better choice of the muffin overlap or the muffin-tin zero potential. However, these choices in an asymmetrical environment remain arbitrary and difficult.

The loss of an inversion center is very important for many physical phenomena. The use of XANES to analyze it can be fruitful if its calculation is sufficiently precise. Therefore, calculations were also performed for another FeO_6 molecule, keeping the perfect oxygen octahedron but displacing the Fe atom by 0.2 Å toward the apical (along z) oxygen.

In this case, the linear dichroism is stronger (Fig. 3). The differences are located in the edge region. When the polarization is perpendicular to the Fe-atom displacement, the NMT calculation is sensitive to this displacement. Conversely, the MT calculation is quite similar irrespective of whether the Fe atom is displaced. Asymmetrical situations also occur when the first atomic shell is not complete

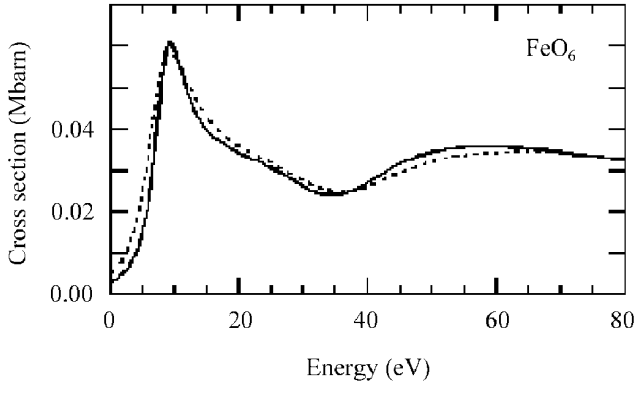

Figure 1
Fe K-edge in a perfect FeO_6 octahedron calculated with muffin-tin (dotted line) and non-muffin-tin (full line) potentials.

around the absorbing atom. Planar situations frequently occur, for instance, in the new superconducting YBaCuO family with its CuO_2 planes. This situation is illustrated with calculations on the FeO_4 molecule where the Fe atom is surrounded by a square of O atoms. The two O atoms along the z direction in the perfect octahedron are eliminated. Interestingly, the main difference between MT and NMT calculations is in the polarization along z; the peak at 10 eV is absent in the MT calculation (Fig. 4). The conclusion is that in the case of low symmetry the muffin-tin MST approach is not able to calculate XANES confidently in the lower energy range.

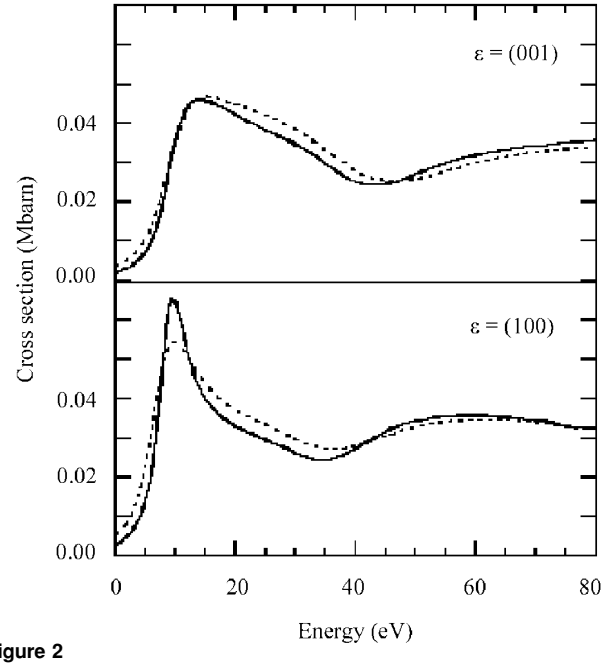

Figure 2
Fe K-edge in the contracted FeO_6 octahedron. The contraction is 10% along the z axis. Full line, NMT; dotted line, MT.

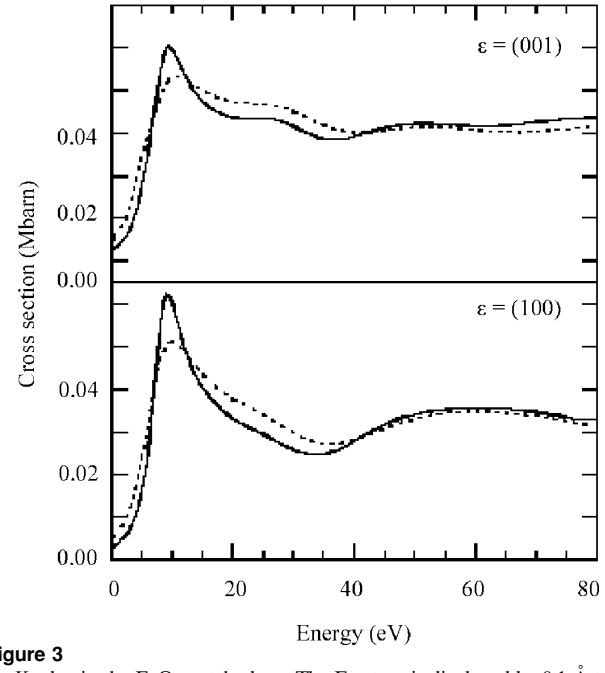

Figure 3
Fe K-edge in the FeO_6 octahedron. The Fe atom is displaced by 0.1 Å toward the apical O atom. Full line, NMT; dotted line, MT.

To conclude this brief presentation of the method, it is stressed that FDM calculations are more time consuming than MST calculations, so the best way to fit or understand experimental data in the lowest-energy part of XANES spectra seems to be to start with MST calculations. Then, in the case of disagreement with experiment, one must continue with FDM calculations. These two approaches are included in the *FDMNES* code (Joly, 2000), which was used for the calculations presented in this paper.

4. Applications

In this section, two examples will be used to illustrate the potential of the method. The first is a K-edge of a 3d metal in an oxide. The problems are quite similar to those encountered in proteins, because the spectra present interesting pre-edge structures that are interpreted with dipolar and quadrupolar transitions, that is, through investigation of the 3d and 4p unoccupied orbitals. The second example illustrates the spectroscopic potential of XANES at very low energy in a small-Z-edge absorption spectra, as can be encountered in organic chemistry.

4.1. The rutile TiO_2

Poumellec *et al.* (1991) measured the Ti K-edge of the rutile TiO_2 for different directions of the electric field and of the propagation vector. Here, we consider two of them: (*a*) $(\varepsilon, \mathbf{k}) = ([001], [110])$ and (*b*) $(\varepsilon, \mathbf{k}) = ([1\bar{1}0], [110])$. We use basis vectors rotated by 45° around the z axis of the conventional crystallographic structure to get the mirror planes along xy, xz and yz. In the structure, there are two kinds of octahedra related to each other by a rotation of 90° around the z axis. The symmetry type of the orbitals reached in the final state in the various experimental setups are (*a*) p_z for the dipolar transition and d_{xz} and d_{yz} for the quadrupolar transitions, and (*b*) p_x and p_y for the dipolar but only d_{xy} for the quadrupolar transitions. According to the ligand field theory applied in our frame, the d_{xy} and d_{yz} orbitals belong to the t_{2g}-like representation; d_{xz} belongs to the e_g-like representation. The result of the fitting is shown in Fig. 5, where the

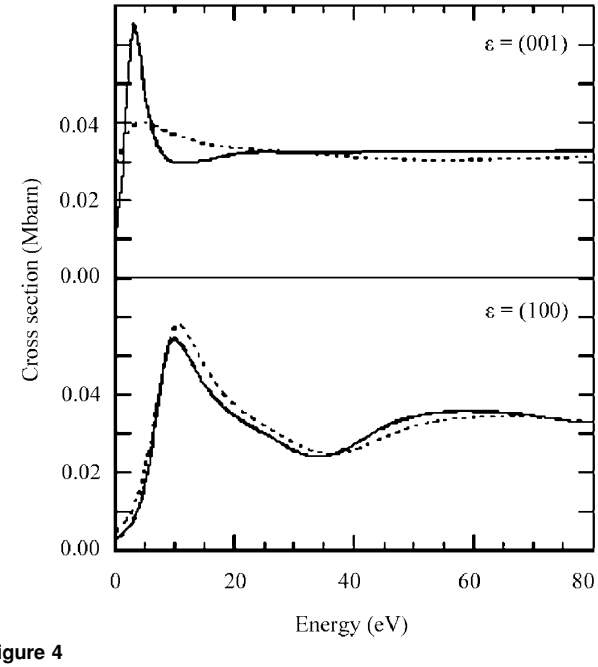

Figure 4
Fe K-edge in the FeO_4 planar molecule. Full line, NMT; dotted line, MT.

experimental and theoretical spectra are superimposed for the two experimental setups (*a*) (top) and (*b*) (bottom).

Cluster size convergence was reached with a radius of 6.9 Å. The agreement between experiment and theory is very good: all the features are well reproduced in amplitude and position and in both orientations. The interpretation of the three peaks (A_1, A_2 and A_3) was controversial. One can observe that A_2 and A_3 are higher when ε is along the *c* axis than when it is perpendicular to it. Conversely, A_1 is lower in the first polarization. One can see that the shape of the A_2 peak is also well reproduced, its width being larger in the second orientation. The quadrupolar contribution is significant; the A_1 peak is only quadrupolar t_{2g}; A_2 is dipolar in nature but includes also a small e_g quadrupolar component; A_3 is a pure dipolar feature.

The purpose of this study was not only the interpretation of XANES peaks but also the evaluation of electronic parameters with a fitting procedure. The adjustable parameters are the Ti 3*d* orbital occupation numbers: n_d^* for the photoabsorber and n_d for the other Ti atoms. n_d^* includes the amount of screening charge on the central atom. The O 2*p* orbital n_p is given by charge neutrality ($n_p = 6 - n_d/2$). No occupation of the 4*s* orbital in titanium was present. The fitting procedure gives $n_d^* = 1.91$, $n_d = 1.00$ and $n_p = 5.50$. The quadrupolar transition is extremely sensitive to the n_d^* parameter, contrary to the dipolar transition. Thus it is the fit of the energy position of peak A_1 that permits the high-accuracy evaluation of n_d^*. A calculation with $n_d = 2.00$ showed that the quadrupolar transition A_1 shifted upward in energy by 2.0 eV, hence with a slope of 2.0 eV per 0.1 electron of screening charge. The fact that the core-hole charge is not completely screened (0.1 electron charge is missing) points to a correlation effect caused by the presence of the excited 3*d* electron that hinders the screening process. The interesting comparison with the same quantity for the dipolar transition cannot be made because of the poor sensitivity of the spectral shape to the screening charge. n_d was optimized with peaks A_2 and A_3 in the experimental spectra, judging from their energy distance from the main edge. Their energy position was quite sensitive to the amount of charge transfer between Ti and O atoms with a derivative of 0.6 eV per tenth of an electron on titanium. This allowed a precise evaluation of the occupation numbers. Also their amplitude variation with polarization did agree with the data. However this parameter affects not only the A_2 and A_3 peaks but also the entire spectrum's shape. These results are in agreement with band-structure calculations performed within the full-potential linearized augmented plane wave (FLAPW) framework. For more details see Joly *et al.* (1999).

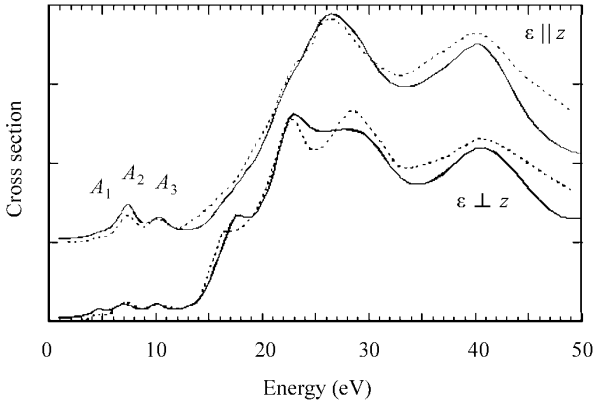

Figure 5
Ti *K*-edge in the TiO_2 rutile. Full line, calculation; dotted line, experiment (Poumellec *et al.*, 1991).

4.2. The acrylonitrile CH_2CHCN

The experiments were performed by Laffon *et al.* (1995) at SuperACO under ultra-high-vacuum conditions. The acrylonitrile multilayers were deposited at 95 K and XANES spectra were recorded at normal and grazing incidence (polarization at 25° to the normal direction). The molecule is planar and the authors showed that these spectra provide symmetry information indicating that the molecule is oriented almost flat on the surface. The authors also used a multiple-scattering $X\alpha$ approach to interpret the different resonances observed from each excited atom of the molecule. Here just the nitrogen *K*-edge is considered, the goal being to illustrate the method not to make a complete study of the molecule.

Therefore, calculations were performed using the FDM approach, the general agreement of the results being far better in this case than when using a multiple-scattering MT calculation. This is confirmed in Fig. 6, where the different structures present in the spectra are assigned. The calculations provide the XANES signal for polarizations along three base directions: one normal to the molecule, *z*, and two in the molecule plane, *x* along the N—C bond direction and *y* perpendicular to it. Owing to the selection rules for a *K*-edge, the *z* direction probes the p_z atomic orbital, that is, the molecular π_z^* orbital. With the bonding orbital being occupied, it is the antibonding orbital that receives the photoelectron. This point is confirmed by considering the amplitudes in the expansion in spherical waves around the N and C neighboring atoms: they have opposite sign. The presence of two thin π_z^* orbitals is found in the calculation at the good energy positions, the second orbital being slightly broader because it is less strongly bounded. Along *y*, only one π_y^* is found. In the *x* direction, the σ_x^* molecular orbitals are investigated. These orbitals are in the continuum (that is, above the vacuum level), which explains their large extension in energy. The splitting of the σ_x^* and π_y^* orbitals is due to the delocalization of the bonding over the entire molecule.

On a more fundamental level, the effect of the core hole was analyzed. Indeed, the photoelectron looks for an excited molecule with a hole at the 1*s* level of the nitrogen photoabsorber. Different calculations were performed with potentials resulting from a non-excited molecule, an excited ionized 1+ molecule with a hole and finally a $Z + 1$ molecule where the absorber is replaced by an O atom,

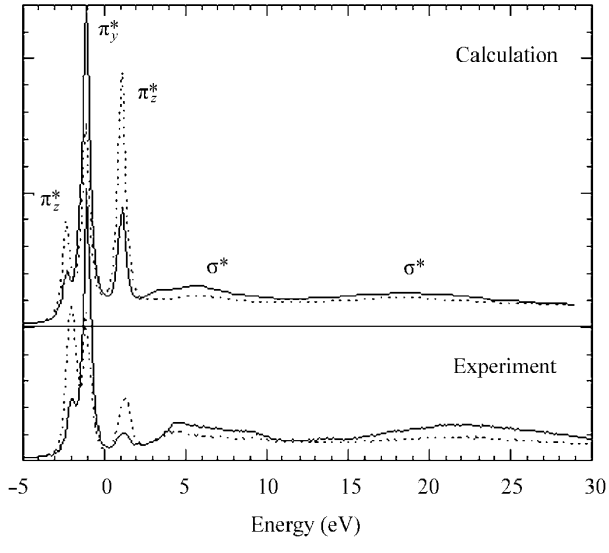

Figure 6
C *K*-edge in the acrylonitrile molecule. Full line, normal; dotted line, grazing. Top, calculation; bottom, experiment (Laffon *et al.*, 1995).

as often occurs in XANES calculations. The electronic configurations were self-consistently calculated and input into the *FDMNES* code to calculate the XANES spectra. The best result, as shown in Fig. 6, comes from the ionized calculation.

5. Conclusion

Low-energy XANES is very sensitive to many parameters and thus care must be taken when interpreting data at very low energies. With this precaution, it can become an excellent tool for analyzing fundamental phenomena that are unreachable by other techniques. It can be applied to metalloproteins, systems that have very similar problems to the metal oxide presented here. The developments presented in this paper must be continued, in particular, with the introduction of magnetism with the spin–orbit coupling and the inclusion of correlated phenomena.

References

Adrait, A., Jacquamet, L., Le Pape, L., Gonzalez de Peredo, A., Aberdam, D., Hazemann, J. L., Latour, J. M. & Michaud-Soret, I. (1999). *Biochemistry*, **38**, 6248–6260.

Ahlers, D., Attenkofer, K. & Schütz, G. (1998). *J. Appl. Phys.* **83**, 7085–7087.

Ahlers, D., Schütz, G., Popescu, V. & Ebert, H. (1998). *J. Appl. Phys.* **83**, 7082–7084.

Akamatsu, K. & Yokoya, A. (2001). *J. Synchrotron Rad.* **8**, 1001–1002.

Ascone, I., Cognigni, A., Le Goudec, J. P. & Itié, J. P. (2000). *High Press. Res.* **19**, 277–283.

Ascone, I., Sabatucci, A., Bubacco, L., Di Muro, P. & Salvato, B. (2000). *Eur. Biophys. J.* **29**, 391–397.

Blaha, P., Schwarz, K., Sorantin, P. & Trickey, S. (1990). *Comput. Phys. Commun.* **59**, 399–415.

Boese, J., Osanna, A., Jacobsen, C. & Kirz, J. (1997). *J. Electron Spectrosc. Relat. Phenom.* **85**, 9–15.

Carravetta, V., Plashkevych, O. & Ågren, H. (1998). *J. Chem. Phys.* **109**, 1456–1464.

Chen, L. X., Utschig, L. M., Laible, P. D., Schlesselman, S. L., Hanson, D. K. & Tiede, D. M. (2000). *Biochemistry*, **39**, 2961–2969.

Della Longa, S., Arcovito, A., Vallone, B., Congiu-Castellano, A., Kahn, R., Vicat, J., Soldo, Y. & Hazemann, J. L. (1999). *J. Synchrotron Rad.* **6**, 1138–1147.

Della Longa, S., Ascone, I., Bianconi, A., Bonfigli, A., Congiu-Castellano, A., Zarivi, O. & Miranda, M. (1996). *J. Biol. Chem.* **35**, 21025–21030.

Della Longa, S., Ascone, I., Fontaine, A., Congiu-Castellano, A. & Bianconi, A. (1994). *Eur. Biophys. J.* **23**, 361–368.

Dill, D. & Dehmer, J. L. (1974). *J. Chem. Phys.* **61**, 692–699.

Ellis, D. E. & Painter, G. S. (1970). *Phys. Rev. B*, **2**, 2887–2898.

Giorgetti, M., Ascone, I., Berretoni, M., Conti, P., Zamponi, S. & Marassi, R. (2000). *J. Biol. Inorg. Chem.* **2005**, 156–166.

Gonis, A., Zhang, X. G. & Nicholson, D. M. (1989). *Phys. Rev. B*, **40**, 947–965.

Huhne, T. & Ebert, H. (1999). *Solid State Commun.* **109**, 577–582.

Huhne, T., Zecha, C., Ebert, H., Dederichs, P. H. & Zeller, R. (1998). *Phys. Rev. B*, **58**, 10236–10247.

Illman, B. L., Bajt, S. & Sutton, T. L. (1994). National Synchrotron Light Source Activity Report BNL 52455. Brookhaven National Laboratory, Upton, NY, USA.

Jacquamet, L., Aberdam, D., Adrait, A., Hazemann, J. L., Latour, J. M. & Michaud-Soret, I. (1998). *Biochemistry*, **37**, 2564–2571.

Joly, Y. (2000). *Fundamental study of the X-ray spectroscoopies at the threshold edge*, http://www-cristallo.polycnrs-gre.fr/simulation.

Joly, Y. (2001). *Phys. Rev. B*, **63**, 125120–125129.

Joly, Y., Cabaret, D., Renevier, H. & Natoli, C. R. (1999). *Phys. Rev. Lett.* **82**, 2398–2401.

Kimball, G. E. & Shortley, G. H. (1934). *Phys. Rev.* **45**, 815–820.

Kitamura, N. & Ektessabi, A. (2001). *J. Synchrotron Rad.* **8**, 981–983.

Laffon, C., Ehrke, H. U., Parent, Ph., Wurth, W. & Tourillon, G. (1995). *Physica B*, **208**/**209**, 56–58.

Meinke, C., Solé, V. A., Pospisil, P. & Dau, H. (2000). *Biochemistry*, **39**, 7033–7040.

Natoli, C. R., Benfatto, M. & Doniach, S. (1986). *Phys. Rev. B*, **34**, 4682–4694.

Park, C. H., Keyhan, M., Wielinga, B., Fendorf, S. & Matin, A. (2000). *Appl. Environ. Microbiol.* **66**, 1788–1795.

Poumellec, B., Cortès, R., Tourillon, G. & Berthon, J. (1991). *Status Solidi B*, **164**, 319–326.

Rehr, J. J., Zabinsky, S. I. & Albers, R. C. (1992). *Phys. Rev. Lett.* **69**, 3397–3400.

Rompel, A., Cinco, R. M., Roblee, J. H., Latimer, M. J., McFarlane, K. L., Huang, J., Walters, M. A. & Yachandra, V. K. (2001). *J. Synchrotron Rad.* **8**, 1006–1008.

Tanaka, M., Nakagawa, K., Koketsu, T., Agui, A. & Yokoya, A. (2001). *J. Synchrotron Rad.* **8**, 1009–1011.

Tyson, T. A., Hodgson, K. O., Natoli, C. R. & Benfatto, M. (1992). *Phys. Rev. B*, **46**, 5997–6018.

Yoshida, S., Ektessabi, A. & Shigeyoshi, F. (2001). *J. Synchrotron Rad.* **8**, 998–1000.

Received 19 December 2001 • Accepted 29 August 2002